Noise properties of HF radar measurement of ocean surface currents

Philippe Forget

AGU PUBLICATIONS

Radio Science

RESEARCH ARTICLE
10.1002/2015RS005681

Key Points:
- Characterization of noise in HF radar-derived surface current measurements
- Impact of noise on the minimum timescale of variability of geophysical currents
- Method to estimate the sampling period for getting data at geophysical level

Correspondence to:
P. Forget,
forget@univ-tln.fr

Citation:
Forget, P. (2015), Noise properties of HF radar measurement of ocean surface currents, *Radio Sci.*, *50*, 764–777, doi:10.1002/2015RS005681.

Received 17 FEB 2015
Accepted 14 JUL 2015
Accepted article online 16 JUL 2015
Published online 11 AUG 2015

Noise properties of HF radar measurement of ocean surface currents

Philippe Forget[1]

[1]Mediterranean Institute of Oceanography, Université de Toulon, Université Aix Marseille, CNRS/INSU, IRD, UM 110, La Garde, France

Abstract High-frequency (HF) radars are commonly used for coastal circulation monitoring. The objective of the study is to assess what is the minimum timescale of variability of the geophysical surface currents that are accessible to the radar measurement given the intrinsic noise of this measurement. Noise properties are derived from the power density spectra (PDSs) of radial current records, which are compared to a model of the PDS of idealized currents contaminated by an additive white noise. The data were collected by two radar systems operating in the Northwestern Mediterranean. Periods of 3 weeks to 7 months are considered. Most of measured currents are affected by a white noise effect. Noise properties vary in time and space and are not specific to a particular radar station or to the radar signal processing method used (beam forming or direction finding). An increase of the noise level reduces the effective temporal resolution of radar-derived currents and then increases the minimum observable timescale of variability of geophysical currents. Our results are consistent with results of comparison found in literature between in situ sensors and radar measurements as well as between two radars operating along a same base line. The study suggests a self-sufficient method, requiring no external data, to estimate the minimum sampling period to consider for getting data sets having a minimized contamination by instrumental noise. This period can also be taken for smoothing or filtering measured currents.

1. Introduction

Ground wave HF radars, developed in the 1970s, are commonly used for the monitoring of coastal circulation. Their contribution to the understanding of the physics of the coastal ocean is significant with important prospects in model assimilation (see the recent review paper of *Paduan and Washburn* [2013]). Radar-derived currents are essentially surface currents with a measurement depth of typically 1 m at 10–15 MHz. The echo from the sea is mainly produced by those surface waves of wavelength equal to half the radar wavelength propagating toward or receding from the radar. These so-called Bragg waves have a known frequency f_{Bragg} and are responsible for two energetic peaks called Bragg peaks. The Doppler shift of the echo is used to measure the phase velocity of these waves and the radial component of the current (we will speak of "radial currents") can be estimated by comparing it with the theoretical value, f_{Bragg}, which is expected in the absence of current [*Barrick et al.*, 1977]. The current radar measurement depends in a known manner on the current profile in the surface layer [*Stewart and Joy*, 1974; *Kirby and Chen*, 1989] and on the sea state via the Stokes drift [*Broche et al.*, 1983; *Ardhuin et al.*, 2009].

Current radar measurements, either radial components (from a single station) or vectors (multiple stations), have been often compared to measurements at sea from mechanical [e.g., *Graber et al.*, 1997; *Nadai et al.*, 1997; *Essen et al.*, 2000] and acoustic current meters [e.g., *Chapman et al.*, 1997; *Teague et al.*, 2001; *Shay et al.*, 2007; *Liu et al.*, 2014; *Jimenez et al.*, 2015]. This approach is, however, limited due to the size, typically kilometric, of radar cells and the specific sensitivity of radar measurements to the structure of the currents within the surface layer of the ocean. This limitation is reduced by the recent use of clusters of drifters released in the radar coverage area [e.g., *Ohlmann et al.*, 2007; *Molcard et al.*, 2009; *Rypina et al.*, 2014]. Finally, internal consistency tests have been conducted using two radars operating on the same baseline [*Yoshikawa et al.*, 2006; *Lipa et al.*, 2006; *Paduan et al.*, 2006].

This study aims to assess what is the minimum timescale of variability of the geophysical surface currents that are accessible to the radar measurement. The method used is self-consistent and does not use in situ data. The study follows our common observation that the morphology of frequency spectra of radial currents generally presents at high frequencies a characteristic aspect of "plateau" which is typical of a white noise

effect. The presence of this plateau profoundly impacts the sensitivity of the radar measurement to variations of the geophysical signal in the high-frequency part of the spectrum. This observation is similar to that recently described by *Xu and Fu* [2012] (see their Figure 1) concerning the wave number spectrum of oceanic sea surface wave height.

A simplified model of a noisy current spectrum is developed in section 2. Experimental data are described in section 3. The analysis of experimental spectra in light of the model gives the results given in section 4 and discussed in section 5. Section 6 is the conclusion.

2. Theoretical Background

The Nyquist-Shannon sampling theorem states that the discretization of a signal with a sampling rate frequency F_s (period T_s) enables to represent the frequency content of the signal at frequencies $f < f_N = F_s/2$ (periods $T > T_N = 2T_s$). f_N is the Nyquist frequency.

We consider a signal u which is the sum of a geophysical signal, u_g, and a white noise. The problem consists in the determination, according to noise characteristics, of the frequency of the shortest harmonic component of u_g that can be extracted from u, i.e., the frequency below which HF radar radial current data can be deemed to give reliable results of use for geophysical applications. This frequency is designated by f_{Ng} and is equal to what we will call the effective bandwidth of the signal. The corresponding period is T_{Ng}. The influence of an increasing noise is to decrease the effective bandwidth and therefore the ability to extract the properties of the geophysical signal at high frequencies.

Signal u represents the radar measurement of the radial component of the surface current, i.e., the projection of the horizontal current vector onto the (radial) direction of observation. This measurement is affected by an uncertainty due to the frequency resolution Δf_D of the sea echo Doppler spectrum from which current velocities are measured. This uncertainty, called frequency resolution noise, is the first cause of noise in radial velocity measurements. Assuming a uniform distribution of the frequency resolution noise from 0 to Δf_D the standard deviation (SD) of this measurement noise is given by

$$\sigma_{\mathrm{FRN}} = \frac{\Delta f_D}{\sqrt{12}}, \tag{1}$$

which gives an SD of the uncertainty of current values given by

$$\sigma_0 = \frac{\lambda \Delta f_D}{2\sqrt{12}}, \tag{2}$$

with λ the radar wavelength. The power density spectrum (PDS) of the contribution, b_0, of the frequency resolution noise to u is flat with a mean value given by

$$m_0 = \frac{{\sigma_0}^2}{f_N}. \tag{3}$$

We generalize the model by considering a uniform white noise, b, of arbitrary amplitude characterized by its SD, and adding to u_g. b includes b_0. By the same reasoning as above, this noise fixes a lower limit to the power spectral density (PSD) of the total signal $u = u_g + b$ given by

$$m_b = \frac{{\sigma_b}^2}{f_N}. \tag{4}$$

A realistic simulation of the PDS of u, $\psi_u(f)$, is done in two steps. First we simulate u_g starting from an idealized spectrum

$$\psi_{u_g}(f) = A f^m, \tag{5}$$

where A is a constant. Then b is simulated by considering the spectrum of the white noise

$$\psi_b(f) = m_b. \tag{6}$$

In both cases the modeled signal is equal to the real part of the sum of the complex amplitudes of harmonic components at discrete frequencies $f_i = i\Delta f_D$, $i = 0, \ldots, N-1$ (N number of samples). The amplitude of a given

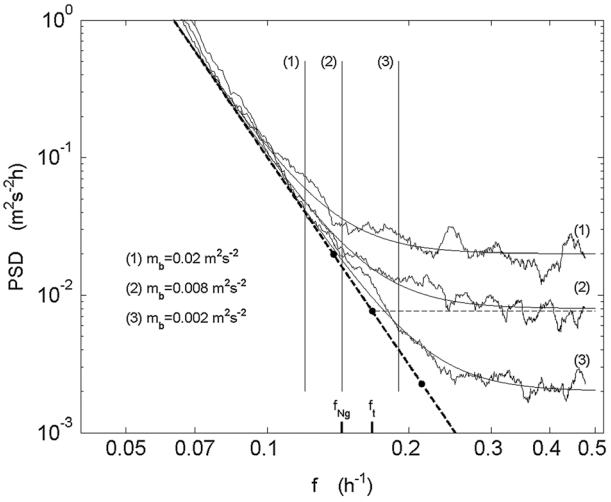

Figure 1. Simulations of the spectrum of a realistic noisy signal u for three values of the spectral noise level m_b. Noisy curves: ψ_u; smooth curves: ψ_{th} (equation (7)); curve in bold dashed line: ψ_{u_g} (equation (5)). u consists of 2048 samples and sampling rate is 1 h. A sliding window of 51 points was applied to ψ_u. The exponent of the frequency power law of ψ_{u_g} is $m = -4$. Heavy points correspond to the intersection of ψ_{u_g} with $\psi_b = m_b$ (equation (6)) (shown for case (2) in thin dashed line). Vertical bars represent estimated effective bandwidths f_{Ng}.

harmonic component is $\sqrt{\psi(f_i)\Delta f_D}\exp -j(2\pi f_i t + \varphi)$, where $\psi(f) = \psi_{u_g}(f)$ or $\psi_b(f)$, and φ is a random number with uniform distribution over the interval 0–2π. Then $\psi_u(f)$ is computed from the sum of the simulated signals.

The model described by equation (5) is partly justified by the well-known Garrett-Munk (GM) spectrum of internal waves [*Garrett and Munk*, 1975] which continues to be a useful description of the oceanic energy spectrum. This model holds from the inertial frequency (17.5 h at latitude 43°N) and the Brunt-Väisälä frequency (typically of 30 mn), i.e., within a range embedding the frequency interval considered. The GM model predicts a fall off of the kinetic energy in the horizontal motions as f^{-2}. Regardless of its physical justification, the model is selected in anticipation of the experimental observation reported in section 4 that there exists almost always a relatively large frequency interval where the energy spectrum of the radial velocity varies according to a power law frequency distribution. The extension of this power law toward higher frequencies up to f_N ($\approx 1\,h^{-1}$) is only hypothetical.

Examples of realistic simulations of $\psi_u(f)$ are shown in Figure 1 for prescribed values of A ($= 7\times10^{-6}\,m^2\,s^{-1}$) and m ($= -4$) and for three values of m_b. The value of m is close to the mean value of measurements (-3.9, see section 4 below). A smoothing using a sliding window of N_s samples is performed to minimize the high variability of spectral amplitudes on the plots in log scale. The theoretical spectra

$$\psi_{th} = \psi_{u_g} + \psi_b \tag{7}$$

are also shown.

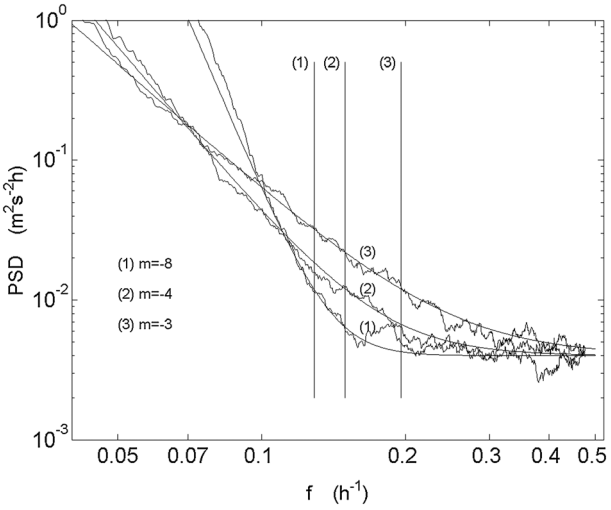

Figure 2. Same as Figure 1 with a constant noise level m_b ($= 0.004\,m^2\,s^{-2}\,h$) and varying m.

The influence of noise on the spectrum is obvious: it determines a lower threshold of spectral amplitudes, equal to m_b, toward which they tend by increasing frequency. This threshold and how the spectra tend to it determine the values of the effective bandwidth and corresponding period. In the examples of the figure, f_{Ng} decreases with increasing m_b. The same holds with increasing $|m|$, m_b being fixed (Figure 2).

An estimate of f_{Ng} we will adopt subsequently is the value $f_{Ng,p}$ of the frequency beyond which the relative difference between ψ_u and ψ_{u_g} is greater than a certain value p. The values of f_{Ng} shown in the figures by vertical lines correspond to $p = 0.5$. This value of p will

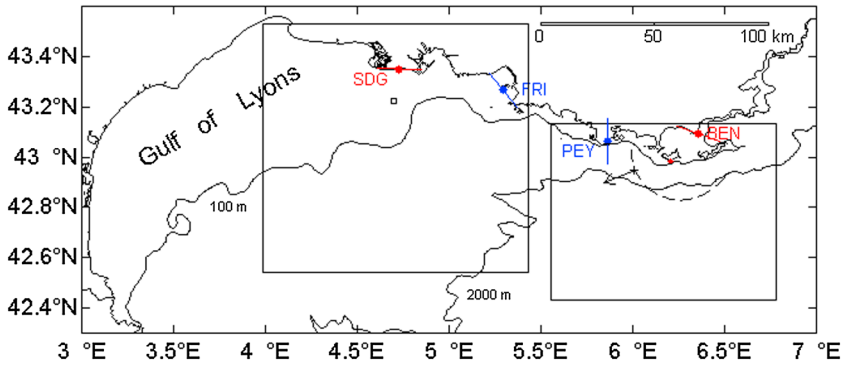

Figure 3. Radar sites. Rectangles correspond to the areas shown in Figures 7–10. The positions of radar stations FRI and SDG (PEY and BEN) of West (East) site are plotted in blue and red, respectively. Segments passing through the stations represent the directions of the receiving arrays. The red dot on Porquerolles Island (east 6.20°, north 42.98°) indicates the transmit radar of the bistatic system formed with the receive station at BEN. The arrow pointing to west-south-west indicates the radial direction of the bistatic radar for a particular cell (cross). The arrow is perpendicular to the ellipse of constant range passing by this point (dashed line). The rectangle south of SDG station locates a particular radar cell which is used in the paper. The 100 m and 2000 m depth contours are plotted.

be taken for f_{Ng} estimations. An upper bound estimator of f_{Ng} is the frequency $f_t = (m_b/A)^{1/m}$ of the intersection point of ψ_{u_g} and ψ_b. Identifying ψ_u with ψ_{th} we obtain

$$f_{Ng,p} = \left(\frac{Ap}{m_b}\right)^{-1/m} = p^{-1/m} f_t \tag{8}$$

3. Experiment

3.1. Overall Description and Data Processing

The data were collected by two dual systems of high-frequency frequency-modulated continuous wave Wellen Radars (WERA) [*Gurgel et al*., 1999]. These systems are installed on two sites in the south of France called West site and East site, respectively (Figure 3). Individual radar stations are referred to FRI, SDG (West site), and PEY, BEN (East site) (these names are acronyms of the places of installation). The West site covers a part of the gulf of Lyons, while the East site covers a deep narrow coastal shelf east of the gulf. The radars have been deployed at these places to study and monitor the coastal circulation on the French coast of the Mediterranean, in general, and the North Mediterranean current in particular. This feature is part of the general cyclonic circulation of the western Mediterranean basin and constitutes a crucial element of the current dynamics in the coastal zone [*Millot and Taupier-Letage*, 2005].

The operating frequency is 16.15 MHz with a bandwidth of 50 KHz. The main specific features of the radars and of operating and processing parameters are given in Table 1. The BEN radar is bistatic, transmit (TX) being made from Porquerolles island and receive (RX) by a linear array located near the coast, 17 km to the northwest. A similar setting was described by *Grosdidier et al*. [2014] with TX made by the radar PEY itself. Isorange lines are then ellipses whose focal points are at the positions O and O' of TX and RX stations, respectively. Under these conditions, the radial distance of a given radar cell located at point M is the distance $(OM + O'M)/2$ and the radial resolution is the distance between two consecutive ellipses.

The receiving arrays are linear except PEY station for which the antennas are arranged zigzag with respect to a north-south axis. The main 3 dB lobe width, δ_w, cannot then be precisely defined.

The West site experiment was earlier (2005–2007) than the East site one (from 2010 to now). The limited number (four) of antennas of radar FRI, due to local constraints, resulted in a low performance in azimuthal resolution, $\delta\phi$, when using the standard beam-forming (BF) method of radar signal processing ($\delta\phi = 30°$). To achieve a satisfactory value of $\delta\phi$, we developed a direction-finding (DF) method based on the multiple signal classification (MUSIC) algorithm [*Schmidt*, 1986]. MUSIC has been routinely used by Coastal ocean dynamics application radars for several years [*Lipa et al*., 2006]. Our algorithm was then applied to SDG data and later on to other radar data, in particular those collected on the East site. For the linear arrays of

Table 1. Main Characteristics of Radars and Data Processing

Site	West Site		East Site	
Period	June 2005 to January 2007		May 2012 to March 2014	
Radar	FRI	SDG	PEY	BEN
Chirp length (τ) (s)	0.325	0.325	0.260	0.260
Number of antenna	4	12	8	8
Array length (m)	26.7	104.5	68	62
Main lobe 3 dB width (δ_w)	30°	9°	-	15°
Processed azimuthal resolution ($\delta\phi$)	5°	5°	2°	2°
Effective (δR) − raw (δR_0) radialresolution (km)	6 − 3	6 − 3	3 − 3	3 − 3
First range (km)	5.5	5.2	8.8	11.9
Number of subseries	20	20	15	15
Acquisition time (T_{i0}) (mn)	22	22	18	18
Acquisition rate (T_a) (mn)	30	30	20	20
Effective integration time (T) (h)	1	1	1	1
Frequency resolution (Δf_D) (Hz)	2.25×10^{-3}	2.25×10^{-3}	1.88×10^{-3}	1.88×10^{-3}

FRI, SDG, and BEN stations, the processed resolution, $\delta\phi$, is significantly less than the 3 dB width, δ_w, of the main lobe of the receiving array (see Table 1).

After processing by the WERA software, the received signal is defined per antenna and per range ring of width δR_0 and corresponds to an acquisition time $T_{i0} = 4096\ \tau$ where τ is the chirp length. A range ring is defined by the surface between two consecutive isorange lines (circles or ellipses, depending on the radar configuration). For statistical and noise considerations, the MUSIC algorithm is expected to work even better when the number of realizations of the complex spectral amplitudes increases. Therefore, MUSIC processing is performed on a set of subseries of the received signal. Subseries correspond to contiguous rings which are grouped to yield an effective radial resolution δR, to an overlapping subdivision of the interval 0–T_{i0} yielding an effective Doppler frequency resolution Δf_D, and to a grouping of these subseries within an effective integration time T greater than the rate of radar acquisition T_a. T is set equal to 1 h. The Nyquist frequency is then $f_N = 0.5\ \mathrm{h}^{-1}$.

The radial currents obtained using MUSIC present, due to the algorithm itself, many outliers. To reduce this drawback, we applied an original outlier-removal algorithm using the histogram of the temporal gradients of the current measured at each radar cell as in *Marmain et al.* [2014]. Other procedures to eliminate nonrealistic measurements could also be envisaged [e.g., *Gomez et al.*, 2014].

For the purpose of analysis, a BF processing was performed for the radar cell of SDG station shown in Figure 3. This radar cell lies within the lobe perpendicular to the array, 15 km south of SDG station. The azimuthal width, of about 2.5 km, is close to that corresponding to the DF processing (1.3 km). The number of grouped rings (2) and subseries (20) are the same as for the DF processing. Radial currents are calculated from the difference between the frequency of the strongest Bragg peak and the theoretical frequency f_{Bragg}.

Table 2 describes the data used. They account for varying periods of 3 weeks to more than 7 months. Only the radar cells having a temporal coverage of at least 90% are selected, data gaps being filled by interpolation. We verified by simulations that imposing such a limit of coverage allows the spectra to be practically insensitive to any interpolation effect. Simulations were similar to those in section 2 where holes of realistic length were introduced randomly in current time series and then filled by interpolation. The total number of these so-called "initial" cells for all selected sequences is 6264.

3.2. Derivation of Theoretical Parameters From Experimental Spectra

The experimental spectra ψ_{exp} are analyzed with reference to the theoretical model ψ_{th} (equations (5)–(7)) with three parameters: the noise spectral amplitude m_b and parameters A and m of the idealized geophysical spectrum ψ_{u_g}.

The value of m_b is estimated by averaging ψ_{exp} in its high-frequency part on the interval $I' = (f_{m_b}, f_N)$ with $f_{m_b} = 0.4\ \mathrm{h}^{-1}$. Attempts were made to improve the determination of the noise floor, for example, using the

Table 2. Sequences of Radar Measurement Used in This Study and Statistical Information for the Selection of the Spectra[a]

Radar	Seq.	Starting Day	*N* Day	n_v	p_1	p_2	p_3	p_4	p_{tot}	n_{tot}
PEY	A	8 July 2012	87	276	100.0	95.3	70.7	65.2	60.5	167
	B	15 March 2013	58	217	89.4	77.9	99.1	87.1	68.7	149
	C	16 May 2013	87	186	98.4	74.2	92.5	85.0	69.9	130
				679						*446*
BEN	D	24 October 2012	88	580	99.0	88.8	82.6	76.9	69.3	402
	E	28 January 2013	129	478	100.0	85.2	81.4	83.7	71.1	340
	F	10 June 2013	87	493	100.0	91.1	72.2	68.4	62.5	308
	G	2 October 2013	52	448	97.8	89.3	92.2	76.3	70.8	317
	H	11 December 2013	83	409	98.3	82.2	90.7	80.0	71.2	291
				2408						*1658*
FRI	I	13 June 2005	21	515	71.5	59.4	70.5	30.9	6.8	35
	J	10 October 2005	46	85	34.1	18.8	68.2	49.4	2.4	2
	K	1 June 2006	53	591	86.3	70.4	58.4	40.3	22.0	130
				1191						*167*
SDG	L	13 June 2005	21	616	94.8	95.3	98.4	69.8	65.8	405
	M	8 September 2005	83	490	98.4	83.7	80.8	74.3	63.7	312
	N	17 December 2005	221	495	100.0	86.1	55.8	80.6	48.9	242
	O	15 November 2006	62	385	99.5	90.4	93.3	80.5	74.8	288
				1986						*1247*

[a]Seq. identifies the sequences and *N* day the number of days of these sequences; n_v is the number of initial radar cells per sequence, p_1–p_4 the percentages corresponding to the C1–C4 criteria used for the selection of the spectra (equation (12)), and p_{tot} the percentage of radar cells satisfying the four criteria at once (number n_{tot}). Numbers in italics indicate the totals.

method of *Hildebrand and Sekhon* [1974], but without substantial benefit. A frequency power law variation of ψ_{exp} consistent with our current spectrum model ψ_{u_g} is almost always observed in some interval *I* above $0.055\,h^{-1}$. The limits of *I*, f_1, and f_2 are computed by varying their values. The solution is the one that achieves an optimal value of the correlation coefficient (*r*) of the regression between $\log\left(\widetilde{\psi}_{exp}\right)$ and $\log(f)$ in the interval *I*, $\widetilde{\psi}_{exp}$ being the smoothed experimental spectrum. Smoothing significantly reduces the weight of very small values of ψ_{exp} in calculations involving its logarithm. The width in number of points of the smoothing window, I_W, is chosen equal to *N*/40 (*N* is the number of samples of the sequence) and varies between 12 and 132. Three constraints are imposed to f_1 and f_2: $f_1 > 0.055\,h^{-1}$, $f_2 < 0.2\,h^{-1}$, $f_2 - f_1 > 0.036\,h^{-1}$. More than 98% of initial radar cells have a correlation coefficient greater than 0.95 in absolute value. The width of the interval *I* (equal to $f_2 - f_1$) corresponding to these cells is between $0.036\,h^{-1}$ and $0.14\,h^{-1}$. Parameter *m* is equal to the slope of the regression above. The values of m_b and *m* being known, the value of *A* is the one that minimizes the cost function $Q(A) = \sum\left(\widetilde{\psi}_{exp} - \psi_{th}\right)^2$ in the interval *I*. We obtain:

$$A = \frac{<\widetilde{\psi}_{exp}(f) - m_b>_I}{<f^m>_I}, \tag{9}$$

where $<\ >_I$ designates the averaging operator over *I*. Due to the determination of *A* (equation (9)), the estimation m_b may differ from the value, m_b', obtained by averaging $\widetilde{\psi}_{exp}(f) - Af^m$ over *I'*, with a relative difference Δ_{m_b}.

We found that a good estimator of the agreement between experimental and modeled spectra was the quantity *q* given by

$$q = \alpha < \left|\log\left(\widetilde{\psi}_{exp}/\psi_{th}\right)\right| >_{I''}, \tag{10}$$

with $I'' = (f_2, f_N)$. The mean absolute difference between $\widetilde{\psi}_{exp}$ and ψ_{th} on a logarithmic scale is *q*. α is introduced so that the measured *q* values are comparable regardless of the width of the smoothing window. It was empirically found from simulations of white noise spectra: $\alpha = \sqrt{I_W}$. We also introduce the quantity q_s defined by

$$q_s = \ < \log\left(\widetilde{\psi}_{exp}/\psi_{th}\right) >_{I''}, \tag{11}$$

which assesses the property of overestimation ($q_s < 0$) or underestimation ($q_s > 0$) of the experimental spectrum by the model.

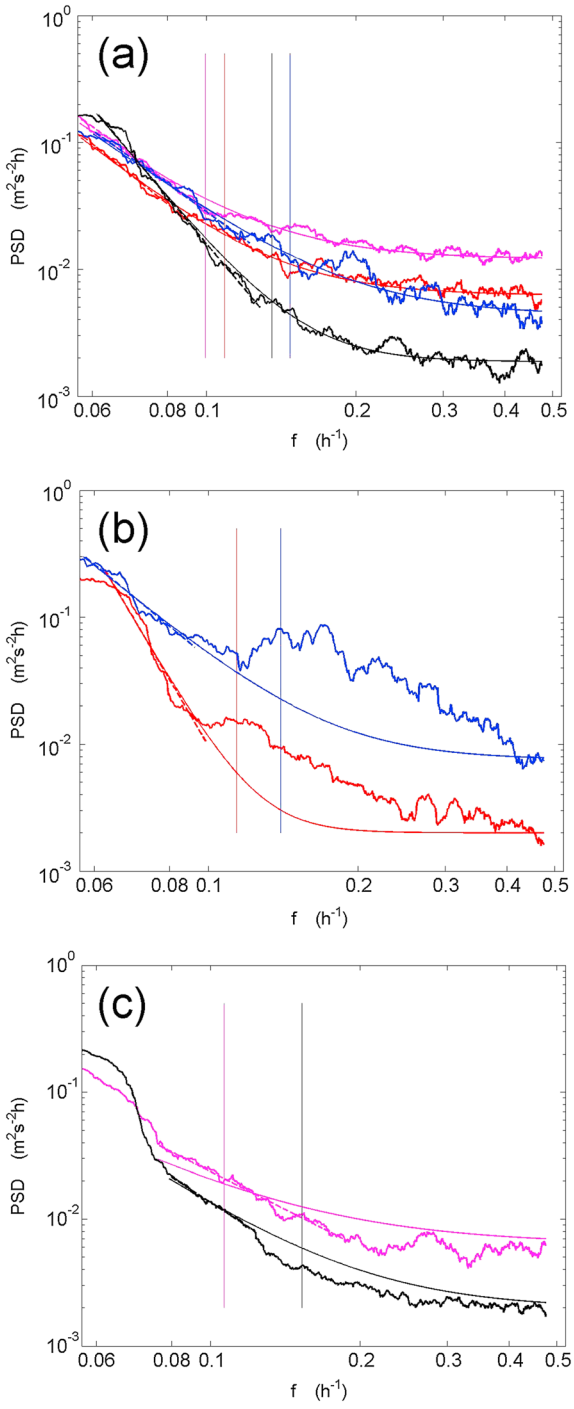

Figure 4. Typical examples of comparison between experimental smoothed ($\widetilde{\psi}_{exp}$, noisy curves) and modeled (ψ_{th}, smooth curves) spectra: (a) good agreement, (b) underestimation, and (c) overestimation of $\widetilde{\psi}_{exp}$ by ψ_{th}. The dashed segments represent the linear regression lines of $\log\left(\widetilde{\psi}_{exp}\right)$ versus $\log(f)$ in the interval $f_1 - f_2$. Vertical bars correspond to effective bandwidths f_{Ng}.

4. Results

Figure 4 shows typical examples of comparison between experimental and modeled spectra. The examples in Figure 4a correspond to a good agreement between $\widetilde{\psi}_{exp}$ and ψ_{th}, whereas in Figure 4b (4c) ψ_{th} underestimates (overestimates) $\widetilde{\psi}_{exp}$ in interval *I*. We observed that cases of underestimation of $\widetilde{\psi}_{exp}$ by ψ_{th} (e.g., Figure 4b, $q_s > 0$) are more numerous than cases of overestimation (Figure 4c, $q_s < 0$) with proportions of 74%, 67%, 60%, and 61% relative to the total number of spectra for stations FRI, SDG, PEY, and BEN, respectively.

The results will be given mainly for the good agreement cases. The matching criteria were investigated by analyzing the value of the parameters introduced in section 2: correlation coefficient *r* of the regression $\log\left(\widetilde{\psi}_{exp}\right)$ versus $\log(f)$ over interval *I*, parameters *q* and q_s and relative deviation Δ_{m_b} between estimated m_b and the value m_b' obtained in section 3.2. The joint observation of experimental and theoretical spectra suggests the following criteria C1–C4:

$$\begin{aligned} &\text{C1: } r > r_{\min} \\ &\text{C2: } |\Delta_{m_b}| < \Delta_{\max} \\ &\text{C3: } q < q_{\max} \\ &\text{C4: } |q_s| < q_{s\max} \end{aligned} \tag{12}$$

with $r_{\min} = 0.97$; $\Delta_{\max} = 0.10$; $q_{\max} = 2.0$; $q_{s\max} = 0.2$. Table 2 gives, for each radar sequence, the percentage of the number of initial cells corresponding to these criteria considered separately and then together. C1 and C2 criteria are generally not penalizing. Applying these two criteria at once, 54%, 88%, 82%, and 87% of radar cells are preserved for stations FRI, SDG, PEY, and BEN, respectively. Adding C3 and C4, the proportions become 14%, 63%, 66%, and 69%. Except FRI station for which only 167 cells are preserved among 1191 initially, these proportions remain significantly high. Radar cells selected by applying C1–C4 criteria will be called "valid" cells. For the spectra in Figure 4a, C1–C4 are satisfied, while only C1 and C2 are satisfied for the spectra in Figure 4b ($q > 3.6$, $q_s > 0.4$) and Figure 4c ($q > 2.4$, $q_s > 0.23$).

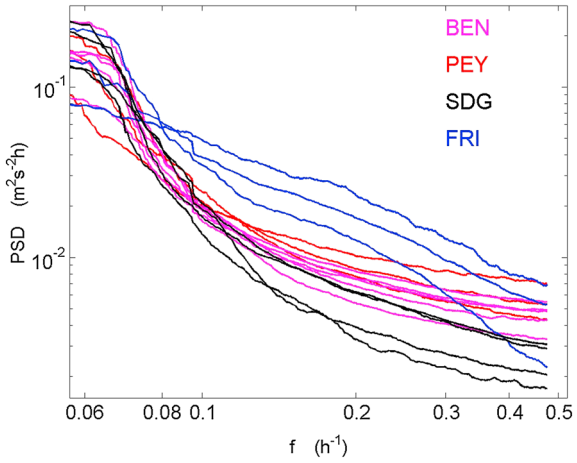

Figure 5. Smoothed averaged experimental spectra. Averaging is performed for each sequence of the set of valid radar cells. Smoothing is done on averaged spectra. The number of summation is the value of n_{tot} in Table 2.

For all the sequences the average temporal coverage and size of data gaps are 97.1% and 7.3 h, respectively. These values do not vary significantly with the sequence. Therefore, we expect a negligible impact on the results of the interpolations made to fill data gaps.

We show in Figure 5 the spectra averaged over the valid radar cells for each experimental sequence. It is observed that the spectra have a morphology qualitatively similar to the model, including a shift toward a constant level around 0.1–0.15 h^{-1}. Furthermore, this level is not only varying between radar stations and sites but also varies with sequences. However, it should be noticed that due to the variability of the spectra, the averaged spectra cannot be reproduced accurately by our model. We also analyzed the spectra of contiguous short (few days) time records within a same sequence. A quite high time variability is observed on model parameters, both in trend and variance, as in the example in Figure 6 (length of subseries: 7 days).

Figures 7–10 show the spatial distributions of m, σ_b, f_{Ng}, and T_{Ng} (= $1/f_{Ng}$), respectively. For m, f_{Ng}, and T_{Ng} we consider only the valid cells defined above. For σ_b, which is estimated independently of the model ψ_{th}, all cells are shown with the exception of those of FRI-K station, which are few. It should be noted in the following that mean values are very close to median values.

The values of m are varying (minimum −8.7, maximum −1.6) with a mean value of −3.9 and a standard deviation SD = 1.2 (Figure 7). We will not comment in the context of this work on the values of m. It should be noted, however, that they are generally different from the value −2 predicted by the GM model (only 9% of the values are equal to -2 ± 0.5). This is not surprising because, first, this model is for open ocean and

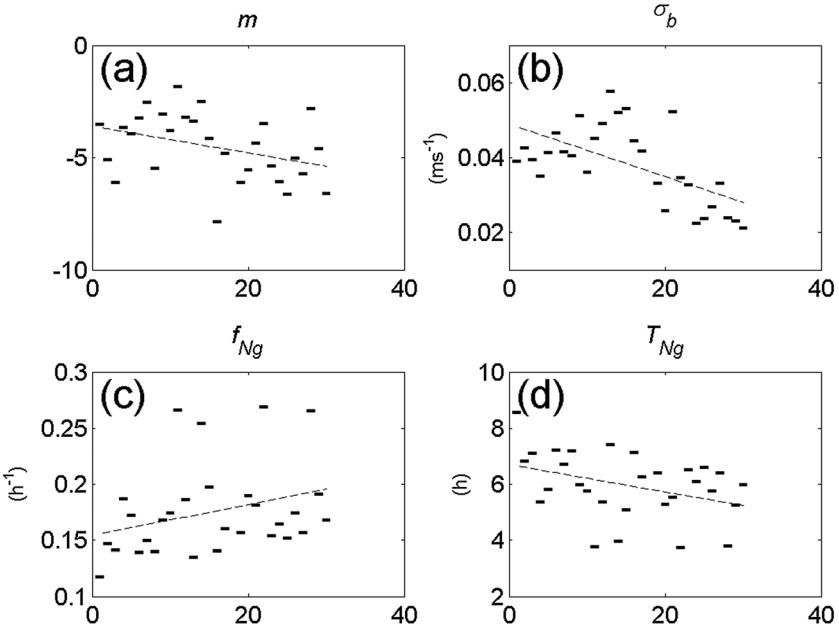

Figure 6. Values of parameters (a) m, (b) σ_b, (c) f_{Ng}, and (d) T_{Ng} for consecutive 7 day periods of time for sequence SDG-N in Table 2 and the radar cell shown in Figure 3. X axis are labeled by the period index.

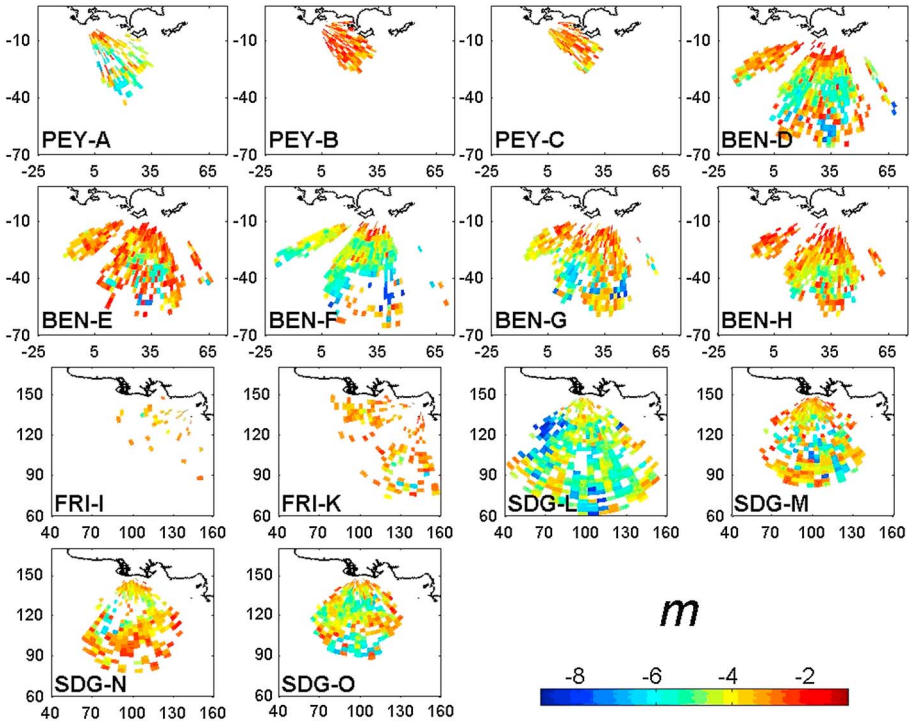

Figure 7. Spatial distribution of the *m* slope characterizing the power law of $\widetilde{\psi}_{exp}$ over interval *I*. Only valid radar cells are shown.

considers ideal conditions (stationarity, isotropy, etc.), and on the other hand, our spectra relate to the radial components of surface currents. The spatial distributions of *m* are heterogeneous and noisy with, in particular, cases of significant difference in the value of *m* in neighboring cells radar. The analysis of a particular example of SDG-M (Figure 11, radar cells distant from 3 km only) explains to a large extent such differences. The experimental spectra are similar, but the automatic determination of the interval showing a decrease of $\widetilde{\psi}_{exp}$ in f^m leads to almost disjoint intervals: in one case (in blue) $I = (0.063, 0.101)\,h^{-1}$ ($r = 0.98$, $m = -7.4$), in the other (in red) $I = (0087–0134)\,h^{-1}$ ($r = 0.99$, $m = -2.6$). The value of *q* is less in the second case (1.0) than in the first one (1.6), which is consistent with the visual observation of a better agreement between $\widetilde{\psi}_{exp}$ and ψ_{th} in the second case. This example, which is often encountered in our data, shows the limits of the methodology, which produces fully satisfactory results only if the spectrum of the current obeys a decreasing power law with constant *m*, whereas in the example, there are two distinct regimes of decrease. Although this has very little influence on the m_b noise level (and thus on σ_b) estimation, it can severely impact the estimation of the effective bandwidth f_{Ng}. More realistic shapes of u_g as well as additional criteria of spectrum selection could be envisaged to improve the accuracy of the method, e.g., as deduced from the analysis of the spectra of in situ current records collected within the radar coverage.

The distribution of σ_b for the PEY station is heterogeneous and seems to vary with the sequence considered (Figure 8). For the BEN station, the distribution is relatively homogeneous except close to the station where σ_b is much larger than at greater distances. It was shown in *Grosdidier et al.* [2014] that bistatic configuration can hinder the estimation of surface currents due to the combined influence of the antenna gains, the variability of f_{Bragg} along isorange ellipses, and the islands. These effects are the most pronounced at the shortest distances from the radar, which can explain the increase of the noise level at these ranges. For FRI and SDG stations, the distribution is fairly uniform but generally varies from one sequence to another. For all the data, the average value of σ_b is $0.042\,m\,s^{-1}$ with a variation interval of $0.018–0.098\,m\,s^{-1}$ ($SD = 0.013\,m\,s^{-1}$). For the actual values of Δf_D, about 2.10^{-3} Hz, we find $\sigma_0 = 5.4 \times 10^{-3}\,m\,s^{-1}$ (σ_0 is due to the frequency resolution, see section 2) which is significantly lower than our experimental measurements of σ_b. Then, it can be concluded that the contribution of the resolution noise to radial velocity measurements is minor.

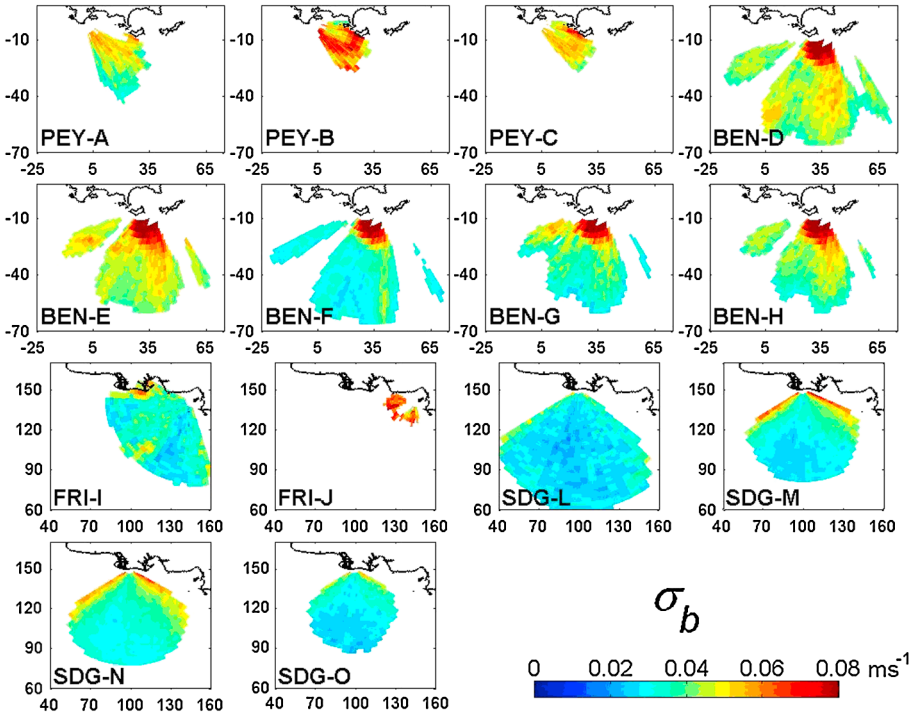

Figure 8. Spatial distribution of the standard deviation σ_b characterizing the amplitude of the noise. All radar cells are shown except those of FRI-K, which are few.

The spatial distributions of f_{Ng} (Figure 9) and T_{Ng} (Figure 10) also show some spatial variability and vary with the sequence considered. The mean value of f_{Ng} is 0.12 h^{-1} with a variation interval 0.07–0.21 h^{-1} (SD = 0.02 h^{-1}). The respective corresponding values for T_{Ng} are 8.2 h, 4.7 h, 14.0 h, and 1.3 h. Choosing the less restrictive definition of the period $T_t = 1/f_t$ (section 2), values become 6.8 h, 3.9 h, 10.3 h, and 1.1 h. Areas of high σ_b values observed for BEN station at short distances correspond to values of T_{Ng} (about 15 h) which are dramatically higher than offshore (a few hours to 10 h). Figure 12 shows that f_{Ng} generally decreases when σ_b (or, equivalently, the noise level m_b) increases. This is in agreement with predictions by our simulations of section 2 (see Figure 1). Equivalently, T_{Ng} increases with σ_b. Moreover, as in simulations of section 2 (see Figure 2) and as it is found, e.g., in Figure 11, f_{Ng} (T_{Ng}) decreases (increases) when $|m|$ increases.

Finally, we compared the potential impact of DF and BF processing on estimates of σ_b and f_{Ng} or T_{Ng}. Figure 13 is a typical example of experimental and modeled spectra obtained by the two processing methods for sequences L-O in Table 2. The example concerns the SDG-N sequence. A remarkable observation is that the spectra are similar, and therefore, the values of σ_b and f_{Ng} or T_{Ng} are similar too. It can be concluded that although very different in principle, the nature of the processing of radar signals (DF or BF) has a low impact on estimated σ_b and f_{Ng} or T_{Ng}.

5. Discussion

Valid cells defined in section 4 show current spectra whose morphology is consistent with the simplified geophysical model (equation (5)) within a range of Doppler frequencies containing the interval I. For frequencies above f_2 the power law can no longer be checked precisely. However, comparison of experimental and theoretical spectra suggests that in this part of the spectrum, the contribution of the geophysical spectrum to ψ_{exp} is from low to negligible compared to noise contribution. This latter dominates and is responsible for the already mentioned plateau effect and therefore for a degradation of the effective temporal resolution of radial velocity measurements. This degradation is even stronger when the noise level is high (Figure 12). We analyzed the spectra obtained by subtracting the noise level m_b (not shown here). The resulting spectra are very noisy at high frequencies and difficult to use, demonstrating the preeminence of the noise to the geophysical signal in this part of the spectrum.

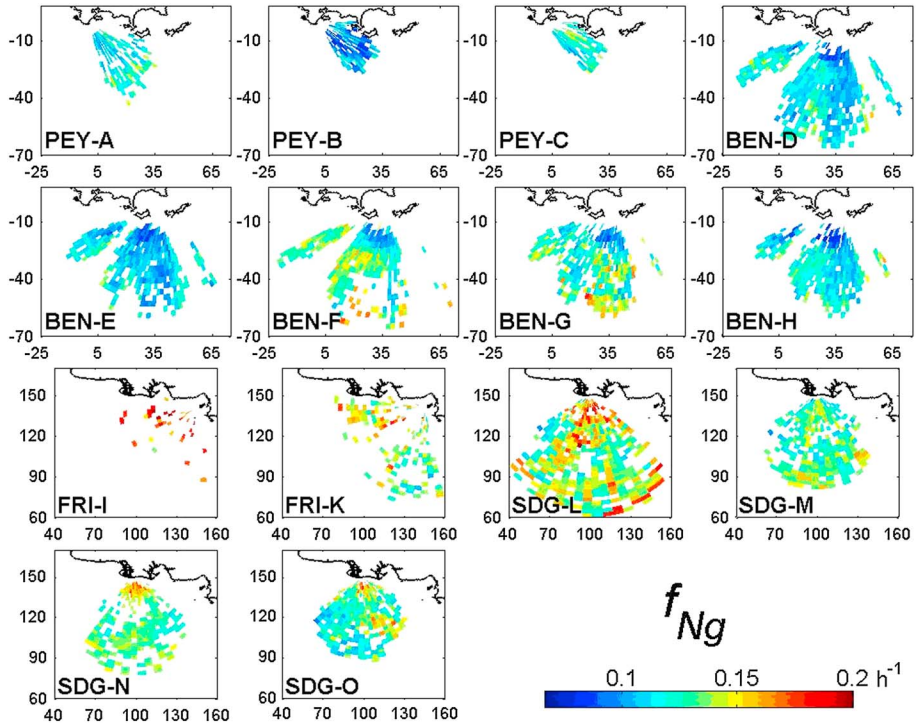

Figure 9. Spatial distribution of the effective bandwidth f_{Ng}. Only valid radar cells are shown.

To our knowledge, the measurement error threshold exhibited by radar-derived current PSDs has been only rarely pointed out [*Wyatt et al.*, 2006; *Liu et al.*, 2010]. In our opinion, it can explain the generally important scatter in "point to point" comparisons between radar and in situ measurements (see references in section 1). Point to point means that these measurements are related to the same temporal resolution,

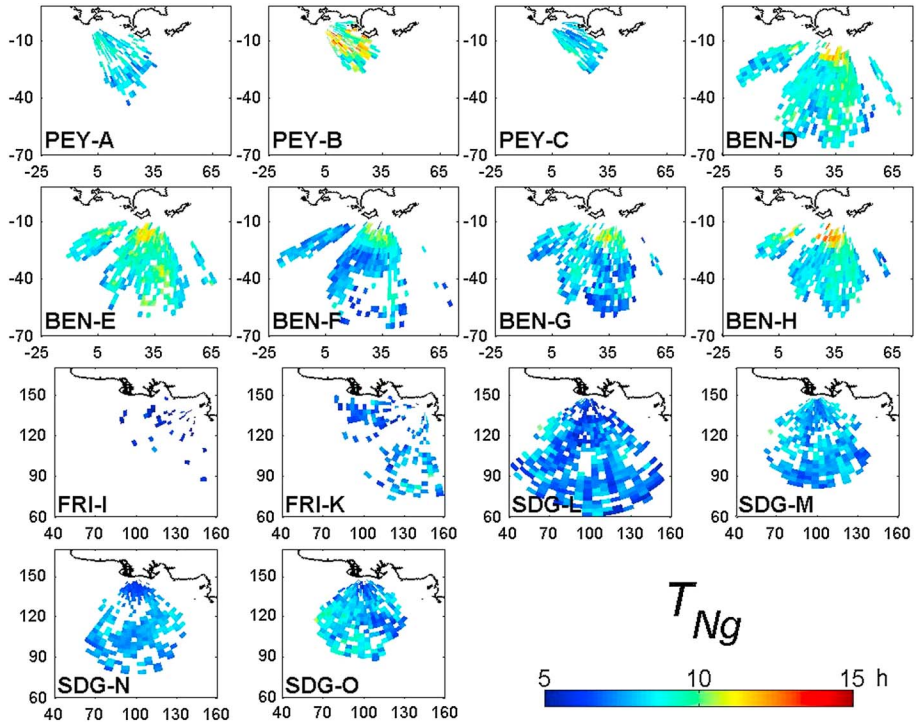

Figure 10. Spatial distribution of the period T_{Ng} corresponding to the effective bandwidth. Only valid radar cells are shown.

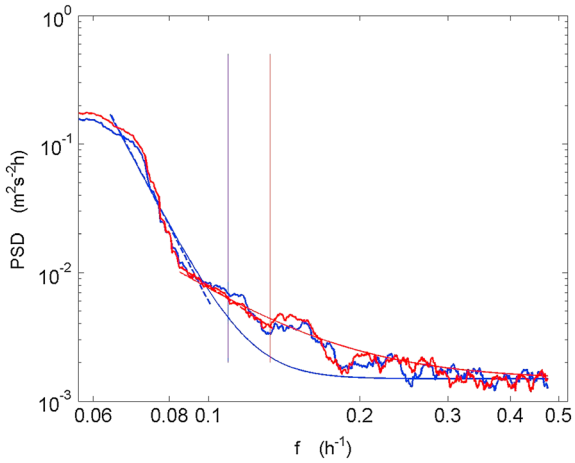

Figure 11. Two examples of smoothed experimental spectra ($\widetilde{\psi}_{exp}$, noisy curves) and corresponding modeled spectra (ψ_{th}, smooth curves) obtained on neighboring cells radar (SDG station sequence *M*). Their positions are (98 km, 103 km) (blue) and (98 km, 100 km) (red). Dashed lines and vertical bars: see Figure 4.

which is that of radar measurements (about an hour). This scatter is reflected by the relatively high values of the error variance, characterized by the root-mean-square difference (RMSD) of these measurements (5–20 cm s^{-1} as reported by *Liu et al.* [2010]).

The scatter is significantly reduced when the temporal resolution is degraded by averaging or by low-pass filtering [*Nadai et al.*, 1997; *Yoshikawa et al.*, 2006; *Lipa et al.*, 2006; *Liu et al.*, 2010; *Rypina et al.*, 2014]. This is also consistent with our effective bandwidth estimates which give temporal resolutions between 5 and 14 h, which is much greater than the hourly resolution of the radar data.

Internal consistency tests consisting of point to point comparisons between radial velocities measured in the vicinity of the middle point of the same base line by facing radars also reveal a significant scatter [*Yoshikawa et al.*, 2006; *Lipa et al.*, 2006; *Paduan et al.*, 2006]. *Yoshikawa et al.* [2006] point out that HF radar error variance can explain much of the RMSDs between radar and acoustic Doppler current profiler measurements. Here too our results, which exhibit a high variability of noise characteristics, are in line with this opinion.

The origin of the intrinsic noise of current radar measurements is not well understood. Exploring the sources of uncertainty, *Lipa et al.* [2006] among others evoke the variability of the radial current within the radar cell and over the duration of the radar measurement, and the statistical noise in the spectral radar data. Radio frequency interferences can also affect the radar signal and add uncertainty to the data [*Merz et al.*, 2015]. Other sources of uncertainty have been identified related to the physics of the measurement (Stokes drift, measuring depth, and specific upper ocean processes) [e.g., *Nadai et al.*, 1997; *Paduan and Rosenfeld*, 1996; *Graber et al.*, 1997] as well as the antenna pattern [*Lipa et al.*, 2006; *Kohut and Glenn*, 2003; *Paduan et al.*, 2006] and spatial and temporal sampling [*Liu et al.*, 2014]. However, we think that these sources of uncertainty are responsible for measurements bias rather than for random noise.

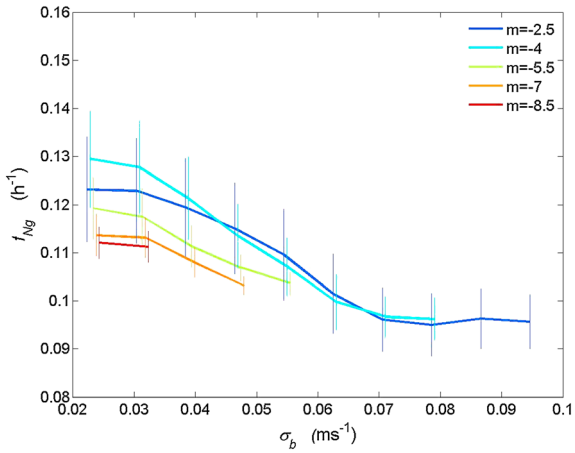

Figure 12. Variation of f_{Ng} with σ_b for different contiguous intervals (width 1.5) of *m* values. The length of the vertical bars is equal to the standard deviation of f_{Ng} in these intervals.

6. Conclusion

The main result of the study is the identification and characterization of noise in radar-derived surface current measurements. This noise is responsible for a plateau in the high-frequency part of Doppler spectra and then can be supposed white. It exhibits a variable level in time and space and is not specific to a particular radar station. We have also shown that for a given radar cell, noise characteristics vary within a given sequence. This noise, which has been rarely pointed out, can have a strong impact on the minimum timescale of

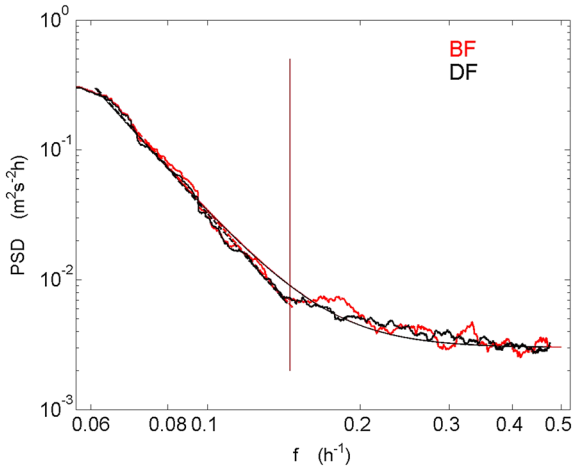

Figure 13. Comparison of smoothed experimental and modeled spectra obtained by processing the radar signals using DF (direction-finding, in black) and BF (beam-forming, red) methods on the radar cell in the coverage area of SDG shown in Figure 3. The selected sequence is sequence *N* from Table 2. Dashed lines and vertical bars: see Figure 4.

variability of geophysical surface currents which can be studied using the HF radar instrument. Depending on the noise level, the effective temporal resolution of radial velocity records for a given cell is reduced.

Whatever the nature of the noise, which is still not well known, our method of analysis provides a simple, self-sufficient method, applying to radar measurements already acquired (postprocessing), requiring no external data, to estimate the minimum sampling period T_{Ng} to consider for getting data sets that can be used for geophysical applications, that is to say having a minimized contamination by instrumental noise. In this perspective, T_{Ng} can be taken as reference for smoothing or filtering issues, e.g., to determine the length of a smoothing window which should be at least of the order of T_{Ng} to provide a reliable geophysical signal. The spatial and temporal variability of the values of parameters σ_b and f_{Ng} or T_{Ng} observed in our measurements demonstrate that the method should be applied for each experimental period and each radar station.

Acknowledgments

This work was supported by Institut National des Sciences de l'Univers-Centre National de la Recherche Scientifique, program LEFE (Les Enveloppes Fluides et l'Environnement) 2013–2014. Radar data have been collected and processed at the Mediterranean Institute of Oceanography (M.I.O.). They are available on request.

References

Ardhuin, F., L. Marié, N. Rascle, P. Forget, and A. Roland (2009), Observation and estimation of Lagrangian, Stokes and Eulerian currents induced by wind and waves at the sea surface, *J. Phys. Oceanogr.*, *39*, 2820–2838.

Barrick, D. E., M. W. Evans, and B. L. Weber (1977), Ocean surface currents mapped by radar, *Science*, *14*, 138–144, doi:10.1126/science.198.4313.138.

Broche, P., J.-C. De Maistre, and P. Forget (1983), Mesure par radar décamétrique cohérent des courants superficiels engendrés par le vent, *Oceanol. Acta*, *6*, 43–53.

Chapman, R. D., L. K. Shay, H. C. Graber, J. B. Edson, A. Karachintsev, C. L. Trump, and D. B. Ross (1997), Intercomparison of HF radar and ship-based current measurements, *J. Geophys. Res.*, *102*, 18,737–18,748, doi:10.1029/97JC00049.

Essen, H.-H., K.-W. Gürgel, and T. Schlick (2000), On the accuracy of current measurements by means of HF radar, *IEEE J. Oceanic Eng.*, *26*(3), 472–480.

Garrett, C., and W. Munk (1975), Space-time scales of internal waves: A progress report, *J. Geophys. Res.*, *80*, 291–297, doi:10.1029/JC080i003p00291.

Gomez, R., T. Helzel, L. Petersen, M. Kniephoff, C. R. Merz, Y. Liu, and R. H. Weisberg, (2014), Real-time quality control of current velocity data on individual grid cells in WERA HF radar, MTS/IEEE Oceans 2014, Taipei, doi:10.1109/OCEANS-TAIPEI.2014.6964502.

Graber, H. C., B. K. Haus, L. K. Shay, and R. D. Chapman (1997), HF radar comparisons with moored estimates of current speed and direction: expected differences and implications, *J. Geophys. Res.*, *102*, 18,749–18,766, doi:10.1029/97JC01190.

Grosdidier, S., P. Forget, Y. Barbin, and C.-A. Guérin (2014), HF bistatic ocean Doppler spectra: Simulation versus experimentation, *IEEE Trans. Geosci. Remote Sens.*, *52*(4), 2138–2148, doi:10.1109/TGRS.2013.2258352.

Gurgel, K.-W., G. Antonischki, H.-H. Essen, and T. Schlick (1999), Wellen Radar (WERA): A new ground-wave HF radar for ocean remote sensing, *Coast. Eng.*, *37*, 219–234.

Hildebrand, P. H., and R. S. Sekhon (1974), Objective determination of the noise level in Doppler spectra, *J. Appl. Meteorol.*, *13*, 808–811.

Jimenez, P., S. Piedracoba, and E. A. Fanjul (2015), Calibration and validation of high-frequency radar ocean surface current observations in the NW of the Iberian Peninsula, *Cont. Shelf Res.*, in press.

Kirby, J. T., and T.-M. Chen (1989), Surface waves on vertically sheared flows: Approximate dispersion relations, *J. Geophys. Res.*, *94*(C1), 1013–1027, doi:10.1029/JC094iC01p01013.

Kohut, J. T., and M. G. Glenn (2003), Improving HF radar surface current measurements with measured antenna beam patterns, *J. Atmos. Oceanic Technol.*, *20*, 1303–1316, doi:10.1175/1520-0426(2003)020<1303:IHRSCM>2.0.CO;2.

Lipa, B., B. Nyden, D. S. Ullman, and E. Terrill (2006), SeaSonde radial velocities: Derivation and internal consistency, *IEEE J. Ocean. Eng.*, *31*(4), 850–861.

Liu, Y., R. H. Weisberg, C. R. Merz, S. Lichtenwalner, and G. J. Kirkpatrick (2010), HF radar performance in a low-energy environment: CODAR SeaSonde experience on the West Florida Shelf, *J. Atmos. Oceanic Technol.*, *27*, 1689–1710.

Liu, Y., R. H. Weisberg, and C. R. Merz (2014), Assessment of CODAR SeaSonde and WERA HF radars in mapping surface currents on the West Florida Shelf, *J. Atmos. Oceanic Technol.*, *31*, 1363–1382.

Marmain, J., A. Molcard, P. Forget, and A. Barth (2014), Assimilation of HF radar surface currents to optimize forcing in the North Western Mediterranean sea, *Nonlinear Process. Geophys.*, *21*, 659–675, doi:10.5194/npg-21-659-2014.

Merz, C. R., Y. Liu, K.-W. Gurgel, L. Petersen, and R. H. Weisberg (2015), Effect of radio frequency interference (RFI) noise energy on WERA performance using the "listen before talk" adaptive noise procedure on the West Florida Shelf, in *Coastal Ocean Observing Systems*, Elsevier, London, U. K., in press.

Millot, C., and I. Taupier-Letage (2005), Circulation in the Mediterranean Sea, *Handb. Environ. Chem., 5K,* 29–66, doi:10.1007/b107143.

Molcard, A., P.-M. Poulain, P. Forget, A. Griffa, Y. Barbin, J. Gaggelli, J.-C. De Maistre, and M. Rixen (2009), Comparison between VHF radar observations and data from drifter clusters in the Gulf of La Spezia, *J. Mar. Syst.*, *78*, S79–S89.

Nadai, A., H. Kuroiwa, M. Mizutori, and S. I. Sakai (1997), Measurement of ocean surface currents by CRL HF ocean surface radar of the FMCW type: Part 1. Radial current velocity, *J. Oceanogr.*, *53*, 325–342.

Ohlmann, C., P. White, L. Washburn, B. Emery, E. Terrill, and M. Otero (2007), Interpretation of coastal HF radar-derived surface currents with high-resolution drifter data, *J. Atmos. Oceanic Technol.*, *24*, 666–680.

Paduan, J. D., and L. K. Rosenfeld (1996), Remotely sensed surface currents in Monterey Bay from shore-based HF radar (Coastal Ocean Dynamics Application Radar), *J. Geophys. Res.*, *101*(C9), 20,669–20,686, doi:10.1029/96JC01663.

Paduan, J. D., and L. Washburn (2013), High-frequency radar observations of ocean surface currents, *Annu. Rev. Mar. Sci.*, *5*, 115–136, doi:10.1146/annurev-marine-121211-172315.

Paduan, J. D., K. C. Kim, M. S. Cook, and F. P. Chavez (2006), Calibration and validation of direction-finding high-frequency radar ocean surface current observations, *IEEE J. Ocean. Eng.*, *31*(4), 862–875.

Rypina, I. I., A. R. Kirincich, R. Limeburner, and I. A. Udovydchenkov (2014), Eulerian and Lagrangian correspondence of high-frequency radar and surface drifter data: Effects of radar resolution and flow components, *J. Atmos. Oceanic Technol.*, *31*, 945–966, doi:10.1175/JTECH-D-13-00146.1.

Schmidt, R. O. (1986), Multiple emitter location and signal parameter estimation, *IEEE Trans. Antennas Propag.*, *34*(3), 276–280, doi:10.1109/TAP.1986.1143830.

Shay, L. K., J. Martinez-Pedraja, T. M. Cook, and B. K. Haus (2007), High-frequency radar mapping of surface currents using WERA, *J. Atmos. Oceanic Technol.*, *24*, 484–503.

Stewart, R. H., and J. W. Joy (1974), HF radio measurements of surface currents, *Deep Sea Res.*, *21*, 1039–1049.

Teague, C. C., J. F. Vesecky, and Z. R. Hallock (2001), A comparison of multifrequency HF radar and ADCP measurements of near-surface currents during COPE-3, *IEEE J. Oceanic Eng.*, *26*(3), 399–405.

Wyatt, L. R., J. J. Green, A. Middleditch, M. D. Moorhead, J. Howarth, M. Holt, and S. Keogh (2006), Operational wave, current, and wind measurements with the Pisces HF radar, *IEEE J. Oceanic Eng.*, *31*(4), 819–834, doi:10.1109/JOE.2006.888378.

Xu, Y., and L.-L. Fu (2012), The effects of altimeter instrument noise on the estimation of the wavenumber spectrum of sea surface height, *J. Phys. Oceanogr.*, *42*, 2229–2233, doi:10.1175/JPO-D-12-0106.1.

Yoshikawa, Y., A. Masuda, K. Marubayashi, M. Ishibashi, and A. Okuno (2006), On the accuracy of HF radar measurement in the Tsushima Strait, *J. Geophys. Res.*, *111*, C04009, doi:10.1029/2005JC003232.